CERMEP-IDB-MRXFDG: A database of 37 normal adult human brain [^{18}F]FDG PET, T1 and FLAIR MRI, and CT images available for research

Inés Mérida[1][*][§], Julien Jung[2,6][*], Sandrine Bouvard[3], Didier Le Bars[1,6], Sophie Lancelot[1,2,6], Franck Lavenne[1], Caroline Bouillot[1], Jérôme Redouté[1], Alexander Hammers[4,5][*], Nicolas Costes[1][*]
*Equal contribution

[1]*CERMEP-Imagerie du vivant, Lyon, France*
[2]*INSERM U1028/CNRS UMR5292, Lyon Neuroscience Research Center, Lyon, France*
[3]*Université Claude Bernard Lyon 1, Lyon Neuroscience Research Center, INSERM, CNRS, France*
[4]*King's College London & Guy's and St Thomas' PET Centre, School of Biomedical Engineering and Imaging Sciences, Kings' College London, London, United Kingdom*
[5]*Neurodis Foundation, Lyon, France*
[6]*Hospices Civils de Lyon, University Hospitals, Lyon France*
[§]*Corresponding author*

Abstract

We present a database of cerebral PET FDG and anatomical MRI for 37 normal adult human subjects (CERMEP-IDB-MRXFDG).

Thirty-nine participants underwent [^{18}F]FDG PET/CT and MRI, resulting in [^{18}F]FDG PET, T1 MPRAGE MRI, FLAIR MRI, and CT images. Two participants were excluded after visual quality control. We describe the acquisition parameters, the image processing pipeline and provide participants' individual demographics (mean age 38 ± 11.5 years, range 23-65, 20 women). Volumetric analysis of the 37 T1 MRIs showed results in line with the literature. A leave-one-out assessment of the 37 FDG images using Statistical Parametric Mapping (SPM) yielded a low number of false positives after exclusion of artefacts.

The database is stored in three different formats, following the BIDS common specification: 1) DICOM (data not processed), 2) NIFTI (multimodal images coregistered to PET subject space), 3) NIFTI normalized (images normalized to MNI space).

Bona fide researchers can request access to the database via a short form.

Keywords: neuroimaging, PET, FDG, MRI, CT, database, healthy subjects, data sharing, BIDS

Introduction

Imaging databases are very useful to re-analyse data in a different context, to increase the number of subjects of a study, and to develop new methods. Imaging databases play a crucial role in numerous analysis methods that rely in the comparison between the data of a group or of an individual and a group of reference. This includes studies using a normative database for analysis and quantification purposes, machine learning approaches, multi-atlas techniques, and validation of image processing pipelines. Databases with different modalities per participant also allow approaches that derive "missing" modalities, e.g. creating pseudo-CTs for attenuation correction in PET-MR (Merida et al. 2017; Burgos et al. 2014; Yaakub, McGinnity, Beck, et al. 2019; Ladefoged et al. 2019).

In the last years, an increasing number of neuroimaging databases has been made available. These databases generally consist of MR images (such as ADNI http://adni.loni.usc.edu, OASIS https://www.oasis-brains.org; for a review see (Coupé et al. 2017)). There is also a large database of PET from the Copenhagen group, CIMBI, containing mainly serotonine receptor PET and associated data (Knudsen et al. 2016). We are aware of very few datasets for [18F]fluorodeoxyglucose ([18F]FDG) PET imaging that have been published (Wei et al. 2018) or are available on request (Archambaud et al. 2013; Eusebio et al. 2012; Alzheimer's Disease Neuroimaging Initiative, ADNI http://adni.loni.usc.edu).

Acquisition of imaging data, such as MRI scanning and in particular PET imaging that requires the injection of a radiotracer, represents an important logistical and monetary cost. In addition, participants have to consent to data acquisition and dissemination, and many countries have restrictions on using ionising radiation in healthy controls, adding to difficulties in acquiring such databases. Database sharing thus contributes to reduce research costs and reduces radiation exposure of healthy controls.

In order to make database sharing more efficient, the scientific community has implemented a database standardisation to organize and describe the data (Brain Imaging Data Structure (BIDS), https://bids.neuroimaging.io, (Gorgolewski et al. 2016)). In this work we introduce a multi-modal database of 37 healthy subjects constructed with MRI, CT and [18F]FDG PET images to BIDS standard. We have obtained ethical permission to share the data on request.

Materials & Methods

Recruitment and cohort characteristics

All enrolled subjects provided written informed consent to participate in the study (EudraCT: 2014-000610-56). The subjects were informed that their anonymized images could be used for methodological development and had been given the option to oppose this use of their data. The inclusion criteria were adult healthy subject and aged between 20 and 65 years. Exclusion criteria were (1) children and adults older than 65 years, (2) woman of childbearing potential without effective contraception, (3) history of neurological disorders, (4) any contraindication for MRI scanning, (5) active infectious disease. Thirty-nine subjects were included in the study. Each subject had a T1-weighted MRI, a T2 fluid-attenuated inversion recovery (FLAIR) MRI and an [18F]FDG PET/CT brain scan. The subjects' MR and PET images were visually reviewed by two neurologists for conspicuous brain abnormalities. Two subjects showing brain lesions on the MR images (one probable insular cavernoma, one cerebellar lesion with hyperintense signal in the FLAIR sequence suggesting possible inflammatory disease of the central nervous system) were excluded from the database.

MRI acquisition and reconstruction

MRI sequences were obtained on a Siemens Sonata 1.5 T scanner. Three-dimensional anatomical T1-weighted sequences (MPRAGE) were acquired in sagittal orientation (TR 2400 ms, TE 3.55 ms, inversion time 1000 ms, flip angle 8°). The images were reconstructed into a 160 x 192 x 192 matrix with voxel dimensions of 1.2 x 1.2 x 1.2 mm^3 (axial field of view 230.4 mm). Sagittal Fluid-Attenuated Inversion Recovery (FLAIR, Hajnal et al. 1993) images (TR 6000 ms, TE 354 ms, Inversion time 2200 ms, flip angle 180°) were acquired with a 176 x 196 x 256 matrix and a voxel size of 1.2 x 1.2 x 1.2 mm^3 (axial field of view 307.2 mm).

PET and CT acquisition and reconstruction

PET and CT data were acquired on a Siemens Biograph mCT64. During the uptake period, participants were instructed to rest with their eyes closed and without auditory stimulation. PET data acquisition started 50 min after the injection of 122.30 ± 21.29 MBq of [^{18}F]FDG (individual doses are provided in the demographics table) and lasted 10 min. PET images were reconstructed using 3D ordinary Poisson-ordered subsets expectation maximization (OP-OSEM 3D), incorporating the system point spread function and time of flight, and using 12 iterations and 21 subsets (Siemens' "HD reconstruction"). Data correction (normalization, attenuation and scatter correction) was fully integrated within the reconstruction process. Gaussian post-reconstruction 3D filtering (FWHM = 4 mm isotropic) was applied to all PET images. Reconstructions were performed with a zoom of 2 yielding a voxel size of 2.04 x 2.04 x 2.03 mm^3 in a matrix of 200 x 200 x 109 voxels (axial field of view 221.27 mm). Low-dose CT images for attenuation correction were acquired with a tube voltage of 100 keV and reconstructed in a 512×512×233 matrix with a voxel size of 0.6 x 0.6 x 1.5 mm^3 (axial field of view 349.5 mm).

Processing pipeline

Data anonymisation and pre-processing

Data anonymisation was performed on the DICOM files using the *gdcmanon* function (http://gdcm.sourceforge.net/html/gdcmanon.html). DICOM files were converted to NIFTI format with *dcm2niix* software (https://github.com/rordenlab/dcm2nii).

The background of CT images was cleaned in order to remove the scanner table and other objects such as the pillow included in the background of the image. For this, a binary mask of the head of the subject was automatically generated following a procedure described in (Merida et al 2015) using tools from the FSL (Version 6.0, https://fsl.fmrib.ox.ac.uk/fsl/fslwiki/) and NiftySeg (http://cmictig.cs.ucl.ac.uk/wiki/index.php/NiftySeg) suites. Finally, the binary mask was applied to the CT image.

Coregistration

As first step, the origin of each NIFTI image was set to the matrix centre. Then, CT, T1 MRI and FLAIR MRI images were coregistered to the [^{18}F]FDG PET image using the *Coregister & Estimate* function from the SPM 12 toolbox (https://www.fil.ion.ucl.ac.uk/spm/software/spm12/).

Spatial normalisation

All images were normalized to MNI space through the tissue classification into grey and white matter probability maps of the T1 image. For that, individual subject's deformation fields were calculated by the *Segment* function of SPM 12,(Ashburner and Friston 2005) from the T1 images previously coregistered to the PET image (but not resliced to preserve native resolution). Transformations for MR to PET space coregistration and PET to MNI space normalisation were concatenated and applied at once to avoid an intermediate resampling of the MRI data. All normalized images were resampled at 1x1x1 mm using 4th degree B-spline interpolation.

Intensity normalisation

Reconstructed PET images were normalized by the subjects' weight and injected dose to obtain Standard Uptake Value (SUV) images (radioactivity concentration [kBq/cm^3] / (dose [kBq] / weight [kg])). In addition, reconstructed PET images were normalized by each subject's mean activity within the intracranial volume (ICV) mask provided by SPM12 to obtain Standard Uptake Value ratio (SUVr).

Regional analysis

The T1 MR images were anatomically segmented into 83 regions using the Hammers_mith maximum probability atlas n30r83, which is based on the mutli-atlas fusion of 30 manually delineated MRIs of healthy young adults (Hammers et al. 2003; Gousias et al. 2008), available at http://brain-development.org. The atlas was wrapped to each individual MRI space *via* the inverse transformation of the deformation fields from subject's space to the MNI space computed at the spatial normalisation step. Grey matter and white matter probability maps obtained with the *Segment* function were thresholded at 0.5 and combined with the 83-ROI anatomical segmentation in order to separate their grey and white matter parts, expect for pure white matter regions like the corpus callosum, and pure grey matter regions like the basal ganglia.

Mean regional SUV and SUVr were extracted in a selection of grey matter anatomical regions of the Hammers_mith segmentation.

Leave-one-out SPM analysis on [18F]FDG images

Leave-one-out ANCOVA was performed on SPM12 in order to compare each subject (healthy control) of the database to the others.
For the statistical analysis, PET images were smoothed with a Gaussian filter at 8mm FWHM. We used age and the global mean calculated within the intracranial volume mask as covariates. Two different contrasts were explored: Hyper-metabolism, i.e. activity of one subject > activity of the remaining subjects in the database, and hypo-metabolism, i.e. activity of one subject < activity of the remaining subjects in the database. Significant differences where defined at $p < 0.05$ FWE at the cluster level.

The database outliers were assessed with three criteria, for both hypometabolism and hypermetabolism.
- Subject-level: number of subjects with significant differences / total number of subjects in the database x 100
- Cluster-level: total number of significant clusters across all subjects / average number of resolution elements (resells) in the mask x 100
- Voxel-level: total number of voxels among the significant clusters across all subjects / number of voxels in the SPM mask x 100

Results

Database IDB-MRXFDG

The final database consists of 37 participants (17 male / 20 female, mean age ± SD, 38.11 ± 11.36 years; range, 23-65 years). Each participant has [18F]FDG PET, T1 MRI, FLAIR MRI, and CT images. An example of coregistered T1, FLAIR, CT and [18F]FDG PET images in the subject space are shown in Figure 1 and the same images in normalized space are shown in Figure 2.
Table 1 summarizes the demographic information for each participant: subject ID, acquisition date, age of the participant at the time of the imaging session, sex, weight, size, injected dose of [18F]FDG, handedness and a comment if any hypersignal was observed on the FLAIR MRI.

The database is available in three different formats, following the BIDS common specification:
- DICOM (data not processed)
- NIFTI (multimodal images coregistered to PET subject space)
- NIFTI normalized (images normalized to MNI space)

Table 2 lists the regional volumes obtained via the Hammers_mith maximum probability atlas. Coefficients of variation were as expected, without obvious outliers. The structure sizes were also in line with expectations (Hammers et al. 2003; Gousias et al. 2008).
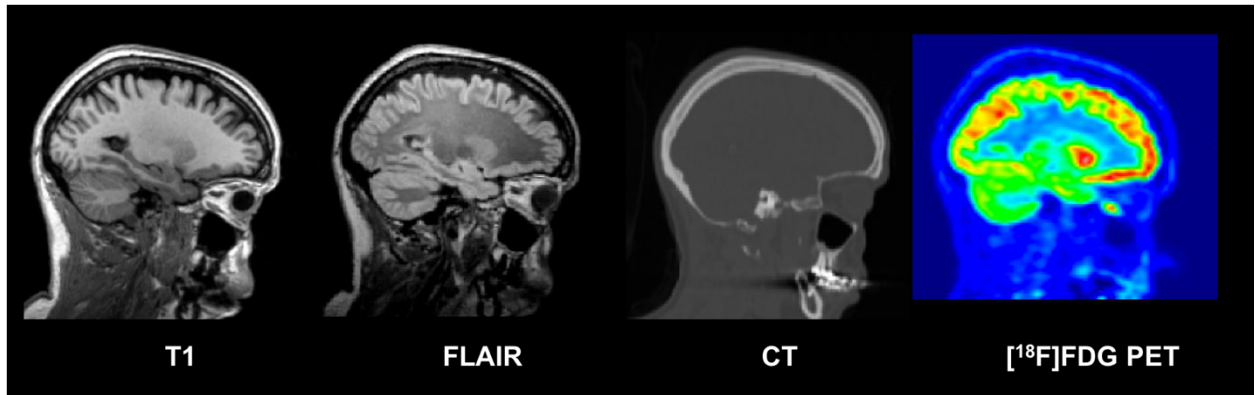

Figure 1: Example of coregistered T1 MRI, FLAIR MRI, CT and [^{18}F]FDG PET images (sagittal plane) for one subject of the database
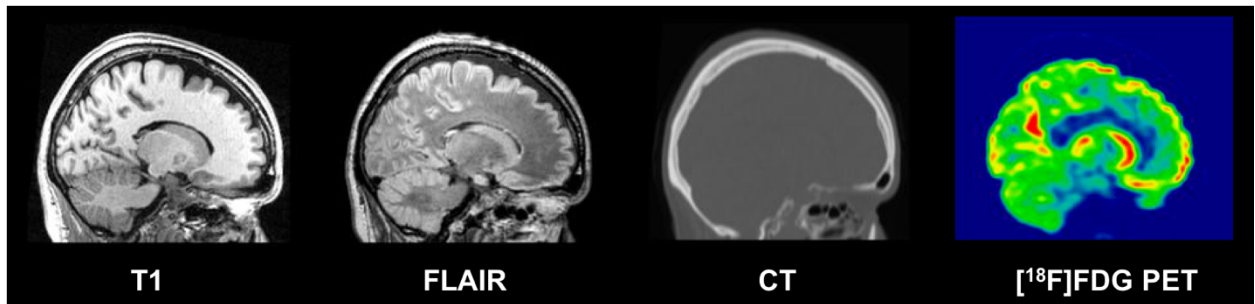

Figure 2: Example of normalized T1 MRI, FLAIR MRI, CT and [^{18}F]FDG PET images (sagittal plane) in MNI space, for one subject of the database

Table 1: Demographics table

Subject ID	Birth date (year)	Age	Sex	Weight (kg)	Size (cm)	Injected Dose (MBq)	Mean activity in ICV mask (MBq)	Handedness
sub-0001	1980	35	F	81	163	149	6911	R
sub-0002	1957	58	F	66	160	102	5781	R
sub-0003	1979	36	M	88	174	144	5980	R
sub-0004	1963	51	M	72	-	124	6551	R
sub-0005	1981	33	M	110	180	147	4925	R
sub-0006	1974	41	M	76	176	119	5590	R
sub-0007	1975	40	F	60	170	118	8271	R
sub-0008	1988	27	F	53	-	95	6889	R
sub-0009	1986	28	F	66	-	135	7974	R
sub-0010	1971	43	M	117	170	168	6137	R
sub-0011	1988	27	F	53	161	99	6944	R
sub-0012	1990	24	F	63	168	123	7911	R
sub-0013	1988	27	M	74	178	135	7798	R
sub-0014 (*)	1964	50	F	55	157	94	2574	R
sub-0015	1981	34	M	62	170	109	6032	R
sub-0016 (*)	1949	65	F	70	170	108	4849	R
sub-0017	1958	56	M	89	185	140	5539	L
sub-0018	1969	45	M	71	168	132	4444	R
sub-0019	1989	25	F	61	161	109	7755	R
sub-0020	1973	42	M	72	185	135	6966	L
sub-0021	1990	25	M	63	178	110	3119	R
sub-0022	1990	25	M	72	178	133	7075	R
sub-0023	1974	41	F	54	168	99	5970	R
sub-0024	1976	39	M	118	199	167	6528	R
sub-0025 (*)	1967	48	F	83	168	149	5811	R
sub-0026	1988	27	F	70	-	134	7656	R
sub-0027	1963	52	F	57	-	107	6647	R
sub-0028	1969	46	F	53	173	95	5481	L
sub-0029	1991	23	M	80	178	136	7824	R
sub-0030	1989	25	M	72	175	124	7384	R
sub-0031	1979	35	F	58	-	112	6621	R
sub-0032	1981	34	M	80	178	136	7011	R
sub-0033	1955	60	F	48	159	95	6151	R
sub-0034	1984	31	F	58	166	106	6119	L
sub-0035	1969	46	F	48	167	96	6066	R
sub-0036	1982	33	M	79	180	149	7253	R
sub-0037	1981	33	F	47	163	92	7355	R
Mean		38.11		70.24	171.81	122	6375	
SD		11.49		17.37	9.11	21	1276	
Min		23		48	157	94	2574	
Max		65		118	199	168	8271	

(*)
sub-0014 : Hyperintense FLAIR signals in white matter (corona radiata) suggesting benign age related white matter hyperintensities (WMHs)
sub-0016 : Hyperintense FLAIR signals in white matter (corona radiata and frontal subcortical structures) suggesting benign age related white matter hyperintensities
sub-0025 : Hyperintense FLAIR signals in white matter (corona radiata and frontal subcortical structures) suggesting benign age related white matter hyperintensities

For those 3 subjects, the location and MRI changes observed in FLAIR sequences are typical findings of WMHs with diffuse areas of high signal intensity (hence, "hyperintense") on T2-weighted or FLAIR sequences. Those WMHs are typically interpreted as a surrogate of cerebral small vessel disease. Due to the high prevalence of those MRI changes in asymptomatic subjects above 50 years, the PET images of those subjects were included in the database.

Regional analysis

Table 2: Regional volumes in native space (in cm³). Each paired region is composed of left and right sub-regions. The short names are expanded in Table A3 in the Appendix.

Structure name	Grey matter	White matter	Structure name	Grey matter	White matter
	Mean ± SD	*Mean ± SD*		*Mean ± SD*	*Mean ± SD*
Temporal Lobe			*Occipital Lobe*		
Hippocampus_r	2.37 ± 0.28	-	OL_rest_lat_l	21.95 ± 2.40	18.27 ± 2.83
Hippocampus_l	2.11 ± 0.26	-	OL_rest_lat_r	22.42 ± 2.54	19.36 ± 3.19
Amygdala_r	1.43 ± 0.17	-	OL_ling_G_l	7.56 ± 0.93	3.94 ± 0.70
Amygdala_l	1.52 ± 0.18	-	OL_ling_G_r	8.16 ± 0.91	3.97 ± 0.79
Ant_TL_med_r	5.48 ± 0.64	1.24 ± 0.28	OL_cuneus_l	5.31 ± 0.66	3.34 ± 0.61
Ant_TL_med_l	5.27 ± 0.61	1.22 ± 0.26	OL_cuneus_r	5.72 ± 0.70	3.09 ± 0.67
Ant_TL_inf_lat_r	2.77 ± 0.39	0.55 ± 0.19			
Ant_TL_inf_lat_l	2.58 ± 0.41	0.49 ± 0.17	*Parietal Lobe*		
G_paraH_amb_r	3.15 ± 0.37	0.98 ± 0.13	PL_rest_l	21.37 ± 2.52	16.01 ± 2.40
G_paraH_amb_l	3.27 ± 0.42	0.99 ± 0.18	PL_rest_r	21.25 ± 2.48	15.95 ± 2.28
G_sup_temp_cent_r	7.62 ± 0.93	5.33 ± 0.79	PL_postce_G_l	11.69 ± 1.58	14.69 ± 1.96
G_sup_temp_cent_l	7.64 ± 0.96	5.26 ± 0.80	PL_postce_G_r	10.80 ± 1.43	13.82 ± 1.76
G_tem_midin_r	11.24 ± 1.33	5.95 ± 0.95	PL_sup_pa_G_l	19.50 ± 2.10	17.65 ± 2.75
G_tem_midin_l	10.78 ± 1.30	5.87 ± 1.03	PL_sup_pa_G_r	20.51 ± 2.15	18.42 ± 3.05
G_occtem_la_r	3.42 ± 0.39	0.92 ± 0.24			
G_occtem_la_l	3.41 ± 0.41	0.94 ± 0.24	*Central Structures*		
PosteriorTL_l	26.41 ± 3.01	17.13 ± 2.44	CaudateNucl_l	4.24 ± 0.52	-
PosteriorTL_r	27.52 ± 3.05	17.48 ± 2.39	CaudateNucl_r	4.33 ± 0.54	-
G_sup_temp_ant_l	3.28 ± 0.42	0.67 ± 0.19	NuclAccumb_l	0.36 ± 0.05	-
G_sup_temp_ant_r	3.19 ± 0.39	0.62 ± 0.17	NuclAccumb_r	0.30 ± 0.04	-
			Putamen_l	4.92 ± 0.57	-
Posterior Fossa			Putamen_r	4.76 ± 0.54	-
Cerebellum_r	44.49 ± 5.10	12.34 ± 1.63	Thalamus_l	7.41 ± 0.87	-
Cerebellum_l	44.36 ± 5.13	12.39 ± 1.63	Thalamus_r	7.25 ± 0.86	-
Brainstem	23.05 ± 2.82	-	Pallidum_l	1.30 ± 0.16	-
			Pallidum_r	1.31 ± 0.16	-
Frontal Lobe			Corp_Callosum	20.83 ± 2.54	-
FL_mid_fr_G_l	23.21 ± 3.01	24.36 ± 3.67	S_nigra_l	0.32 ± 0.04	-
FL_mid_fr_G_r	23.59 ± 2.95	24.52 ± 3.57	S_nigra_r	0.32 ± 0.04	-
FL_precen_G_l	13.11 ± 1.76	18.47 ± 2.32			
FL_precen_G_r	13.04 ± 1.84	18.55 ± 2.37	*Ventricles*		
FL_OFC_AOG_l	3.87 ± 0.51	1.45 ± 0.39	BodyVentricle_r	7.31 ± 1.01	-
FL_OFC_AOG_r	3.89 ± 0.51	1.45 ± 0.35	BodyVentricle_l	7.98 ± 1.01	-
FL_inf_fr_G_l	10.63 ± 1.34	5.96 ± 1.12	TemporaHorn_r	0.63 ± 0.08	-
FL_inf_fr_G_r	10.15 ± 1.24	5.50 ± 1.05	TemporaHorn_l	0.49 ± 0.06	-
FL_sup_fr_G_l	27.15 ± 3.58	20.00 ± 3.10	ThirdVentricl	0.94 ± 0.13	-
FL_sup_fr_G_r	27.33 ± 3.63	19.71 ± 3.12			
FL_OFC_MOG_l	3.95 ± 0.53	1.83 ± 0.37	*Insula and Cingulate gyri*		
FL_OFC_MOG_r	3.93 ± 0.48	1.63 ± 0.30	Insula_l	15.42 ± 1.77	-
FL_OFC_LOG_l	2.13 ± 0.31	0.92 ± 0.22	Insula_r	15.37 ± 1.79	-
FL_OFC_LOG_r	2.39 ± 0.37	0.91 ± 0.24	G_cing_ant_sup_l	5.56 ± 0.74	1.66 ± 0.43
FL_OFC_POG_l	3.14 ± 0.41	1.34 ± 0.28	G_cing_ant_sup_r	5.29 ± 0.69	1.67 ± 0.40
FL_OFC_POG_r	3.27 ± 0.38	1.20 ± 0.27	G_cing_post_l	5.07 ± 0.67	2.52 ± 0.46
FL_strai_G_l	2.69 ± 0.34	0.60 ± 0.13	G_cing_post_r	4.95 ± 0.60	2.36 ± 0.43
FL_strai_G_r	2.88 ± 0.34	0.77 ± 0.20			
Subgen_antCing_l	0.78 ± 0.13	0.59 ± 0.10			
Subgen_antCing_r	0.69 ± 0.13	0.54 ± 0.10			
Subcall_area_l	0.21 ± 0.04	0.02 ± 0.01			
Subcall_area_r	0.18 ± 0.03	0.02 ± 0.01			
Presubgen_antCing_l	0.76 ± 0.11	0.11 ± 0.05			
Presubgen_antCing_r	0.50 ± 0.07	0.08 ± 0.05			

Figure 3 and Figure 4 show boxplots of mean regional SUV and SUVr respectively, extracted in a selection of grey matter anatomical regions, for all subjects in the database. Each region is composed of left and right sub-regions. Mean regional SUV values were 5.36 ± 1.32, range 1.35 - 8.54 (Figure 3). Three subjects in the database had lower SUV values (between 1.35 to 3).
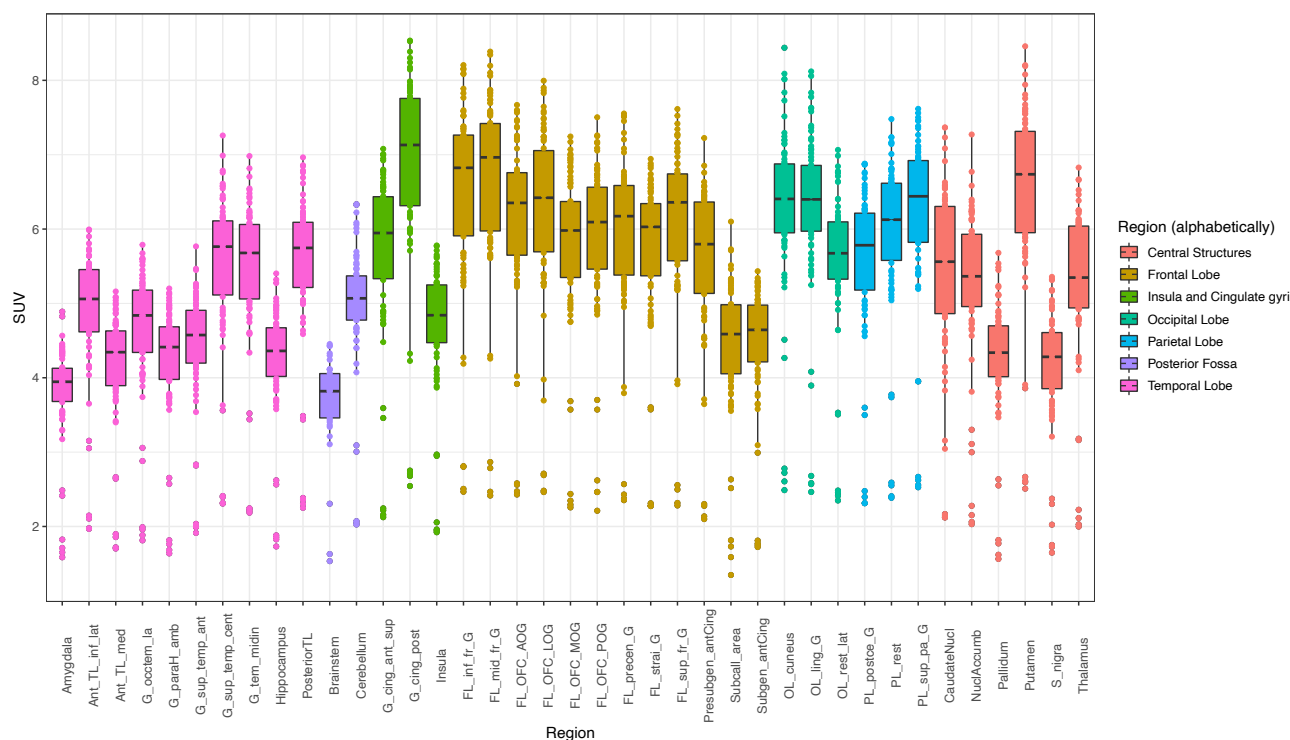

Figure 3: Boxplot of regional SUV for all subjects in the database. Centre lines correspond to medians, boxes to interquartile ranges, and whiskers to robust ranges. Outliers are represented as dots. Each dot represents a participant for unpaired regions and a participant's right or left SUV value for paired regions.

The distribution of SUVr values (Figure 4) remains very similar to the distribution of SUV values (1.49 mean ± 0.26 SD, range 0.85 - 2.22), except that the dispersion is reduced and the outlier values from the three participants with unusually low SUVs are regularized.
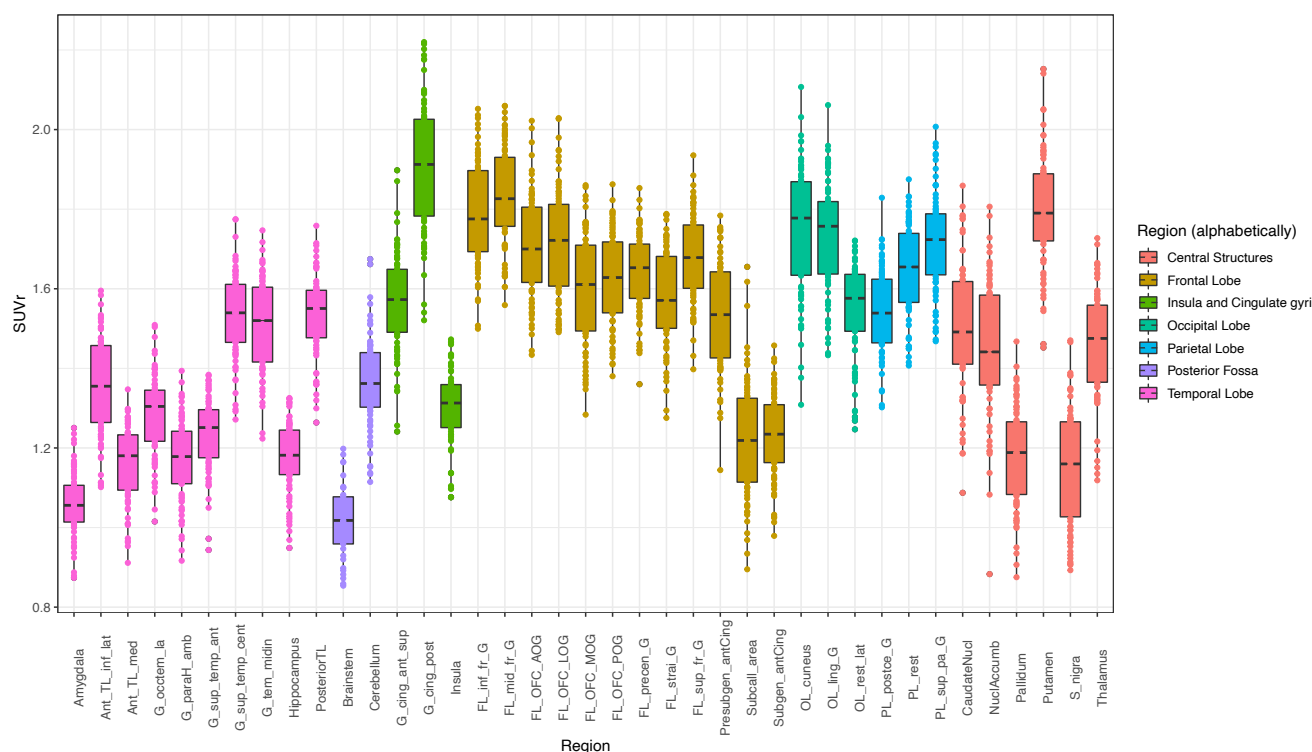
Figure 4: Boxplot pf regional activity normalized by mean activity in ICV mask (SPM) for all subjects in the database. Centre lines correspond to medians, boxes to interquartile ranges, and whiskers to robust ranges. Outliers are represented as dots.

Normalizing with the ICV mean value thus acts as an efficient way for regularizing the SUV distribution leaving the inter-regional variability intact.

Leave-one-out SPM analysis

Results for the leave-one-out analysis of [18F]FDG PET are reported in Table 2.

At the subject-level, 5/37 (13.5%) of the participants had any significant increases in [18F]FDG uptake (hypermetabolism) relative to the other 36 participants. Any significant decreases (hypometabolism) was found for 11/37 (29.7%) of the participants.

At the cluster-level, significant changes were found in at most 5.21% of resolution elements, and at the voxel-level, in at most 0.32% of voxels.

Table 2: % of abnormality in the database. Cluster-level and voxel-level results are reported at p < 0.05 FWE. The denominator for subject-level is the total number of participants; the denominator for the cluster-level is the average number of resolution elements in the mask; the denominator for the voxel-level is the number of voxels in the SPM mask. See Methods for details.

Contrast	Subject-level	Cluster-level	Voxel-level
Hypermetabolism	13.5% (n=5)	0.93%	0.03%
Hypometabolism	29.7% (n=11)	5.21%	0.32%

All abnormalities in controls compared with controls are by definition false positives. We examined all 16 and present our findings in the Appendix (Table A1 and Table A2). Virtually all false positives had an anatomical or artefactual explanation.

Discussion

A new database of 37 healthy subjects including T1 and FLAIR MRI, CT, and [18F]FDG PET images, called IDB-MRXFDG, has been created.

The age range has been selected to reflect the ages of participants in cognitive and clinical research studies at the CERMEP imaging centre, encompassing amongst others epilepsy, movement disorders, multiple sclerosis and disorders of consciousness and will align with the research priorities of many similar centres.

We performed quality control of all images visually and by screening for volumetric and regional SUV abnormalities. Three subjects had unusually low SUVs; this may be due to imperfect observation of the need for fasting ahead of the scan. We show that a simple global normalisation procedure removes the resulting outliers (Figure 4); depending on the application more sophisticated intra-scan normalisation procedures are conceivable (Yakushev et al. 2009, 2008). We also performed SPM leave-one-out studies for [18F]FDG. The relatively high false-positive rates per subject are explained by the existence of significant clusters of small size (from 1 to 95 voxels). Areas of apparent hypermetabolism were either at the edge of the brain or at the bottom of a particularly deep sulcus (see appendix, Table A1); areas of apparent hypometabolism (Table A2) were clearly linked to the participant's anatomy, typically to a wide sulcus or fissure (7/11 cases). The other 4 cases were extracerebral or at the edge of the brain, probably linked to imperfect normalisation. We believe none would have been considered abnormal had they been seen in an analysis comparing one research subject with a particular condition against a group of controls. When testing the normality of the database at the cluster and voxel-level, the expected threshold of 5% of abnormality or lower was found for both hyper- and hypo-metabolism. The database therefore appears suitable for voxel-based [18F]FDG PET analysis with a ≤5% risk of Type 1 error.

The IDB-MRXFDG database could be used in many different applications such as the statistical comparison of a patient (or group of patients) to a database of healthy subjects, automatic quantitative analyses, and more generally methodology development in neuroimaging.

The inclusion of [18F]FDG PET in IDB-MRXFDG is particularly important. While there are now many MR databases covering, with varying density, the human lifespan as reviewed in (Coupé et al. 2017) , we are aware of very few [18F]FDG PET databases. Wei et al. (Wei et al. 2018) scanned 78 healthy subjects aged 3-78 years on a PET/CT scanner; it is not clear whether this database is available on request, and there is no mention of MRI. The Marseille database (used e.g. in (Eusebio et al. 2012)) contains data from 60 healthy adults aged 21-78; [18F]FDG PET, T1 weighted MRI, and CT data are available by arrangement. A rare paediatric database (Archambaud et al. 2013) contains 24 datasets of participants aged 4.5-17.9 years (mean ± SD 10.06 ±3.1 years) and may be shared on request. These are "pseudo-controls" derived from epilepsy patients, selected from among a total of 71 children as the subgroup with both a normal visual analysis and a normal SPM analysis derived iteratively. They have been scanned on a traditional PET scanner with transmission-based attenuation correction which makes comparison with PET/CT data difficult (Sousa et al. 2020); no MRI is available. A large database available on request is the Alzheimer's Disease Neuroimaging Initiative, ADNI (http://adni.loni.usc.edu/about/) which comprises over 300 healthy control [18F]FDG PET datasets; however, participants are aged 55-90 and therefore more suited to dementia research but outside the typical age range used for studies in normal cognition or epilepsy, one of the main clinical indications for clinical brain FDG PET. Similar concerns about the age of participants apply to those databases from the world-wide ADNI (WW-ADNI) networks that do contain FDG, as for example the Japan ADNI (J-ADNI; age 60-84) (Iwatsubo et al. 2018).

Examples of database uses for work in MR include the *voxel-wise* comparison of a patient with a control group to detect abnormalities from T1 images via voxel-based morphometry (Ashburner and Friston 2000; Richardson et al. 1997) and its variants that use T1 derivatives like grey-white matter junction images (Antel et al. 2002; Huppertz et al. 2005) for the detection of specific pathologies like Focal Cortical Dysplasia. FLAIR as a sequence highly sensitive to pathology has similarly been used at the single-subject level in comparison to control groups (e.g. (Focke et al. 2008; Huppertz et al. 2011)). Another group of examples is the *region-wise* comparison of the size of cerebral structures between groups or between individuals and a control group (e.g. (Heckemann et al. 2011; Hammers et al. 2007; Sapey-Triomphe et al. 2015; Klein-Koerkamp et al. 2014)). Importantly, such work has been successfully undertaken with control groups scanned on a different scanner (e.g. (Cross et al. 2013; Yaakub et al. 2020)), and IDB-MRXFDG could be used to increase the size of control groups.

Since PET-CT scanners rapidly displaced PET-only scanners in the early 2000s, low-dose CT has been coupled to brain [^{18}F]FDG PET for estimation of tissue density and attenuation correction. With the advent of commercial PET-MR scanners since 2011, there has been no direct way of measuring electron density in the head, and alternative approaches have had to be found. Synthesis of "pseudo-CTs" via atlas approaches (Burgos et al. 2014; Merida et al. 2017) is a successful approach that performs well overall (Ladefoged et al. 2017) but requires pairs of MR and CT images to achieve the synthesis. IDB-MRXFDG has already been used for such approaches (Merida et al. 2015).

The latter application of databases – MR-based attenuation based on MR-CT pairs – is one domain where Deep Learning methods, notably with Convolutional Neuronal Networks, have recently become very successful (Ladefoged et al. 2020; Yaakub, McGinnity, Beck, et al. 2019). However, they often require substantially larger training datasets or priors than multi-atlas methods, in the case of MR-based attenuation recently estimated at 100-400 pairs, with an influence of MR heterogeneity (Ladefoged et al. 2020). More widespread availability of databases will further Deep Learning approaches, particularly when multiple modalities are available per subject, allowing e.g. synthesis of missing modalities (Yaakub, McGinnity, Clough, et al. 2019) .

Data sharing

We have obtained Ethical permission to make the database available on request for *bona fide* research. Please email (merida@cermep.fr) for a short access form, detailing which format you require (DICOM format, NIFTI in subject's space and NIFIT in normalized space, following BIDS common specification). Your request will then be considered by the access committee. If found in line with permitted use (i.e. *bona fide* research) a licence will be issued and the requested database transferred securely.

References

Antel, Samson B, Andrea Bernasconi, Neda Bernasconi, D.Louis Collins, Robert E Kearney, Rajjan Shinghal, and Douglas L Arnold. 2002. "Computational Models of MRI Characteristics of Focal Cortical Dysplasia Improve Lesion Detection." *NeuroImage* 17 (4): 1755–60. https://doi.org/https://doi.org/10.1006/nimg.2002.1312.

Archambaud, Frederique, Viviane Bouilleret, Lucie Hertz-Pannier, Philippe Chaumet-Riffaud, Sebastian Rodrigo, Olivier Dulac, Francine Chassoux, and Catherine Chiron. 2013. "Optimizing Statistical Parametric Mapping Analysis of 18F-FDG PET in Children." *EJNMMI Research* 3 (1): 1–10. https://doi.org/10.1186/2191-219X-3-2.

Ashburner, John, and Karl J. Friston. 2000. "Voxel-Based Morphometry - The Methods." *NeuroImage* 11 (6 I): 805–21. https://doi.org/10.1006/nimg.2000.0582.

Ashburner, John, and Karl J Friston. 2005. "Unified Segmentation." *NeuroImage* 26 (3): 839–51. https://doi.org/https://doi.org/10.1016/j.neuroimage.2005.02.018.

Burgos, Ninon, M. Jorge Cardoso, Kris Thielemans, Marc Modat, Stefano Pedemonte, John Dickson, Anna Barnes, et al. 2014. "Attenuation Correction Synthesis for Hybrid PET-MR Scanners: Application to Brain Studies." *IEEE Transactions on Medical Imaging* 33 (12): 2332–41. https://doi.org/10.1109/TMI.2014.2340135.

Coupé, P, G Catheline, E Lanuza, and JV Manjón. 2017. "Towards a Unified Analysis of Brain Maturation and Aging across the Entire Lifespan: A MRI Analysis." *Hum Brain Mapp* 38 (11): 5501–18.

Cross, J Helen, Ruchi Arora, Rolf A Heckemann, Roxana Gunny, Kling Chong, Lucinda Carr, Torsten Baldeweg, et al. 2013. "Neurological Features of Epilepsy, Ataxia, Sensorineural Deafness, Tubulopathy Syndrome." *Developmental Medicine & Child Neurology* 55 (9): 846–56. https://doi.org/10.1111/dmcn.12171.

Eusebio, Alexandre, Jean Philippe Azulay, Mathieu Ceccaldi, Nadine Girard, Olivier Mundler, and Eric Guedj. 2012. "Voxel-Based Analysis of Whole-Brain Effects of Age and Gender on Dopamine Transporter SPECT Imaging in Healthy Subjects." *European Journal of Nuclear Medicine and Molecular Imaging* 39 (11): 1778–83. https://doi.org/10.1007/s00259-012-2207-8.

Focke, Niels K, Mark R Symms, Jane L Burdett, and John S Duncan. 2008. "Voxel-Based Analysis of Whole Brain FLAIR at 3T Detects Focal Cortical Dysplasia." *Epilepsia* 49 (5): 786–93. https://doi.org/10.1111/j.1528-1167.2007.01474.x.

Gorgolewski, Krzysztof J, Tibor Auer, Vince D Calhoun, R Cameron Craddock, Samir Das, Eugene P Duff, Guillaume Flandin, et al. 2016. "The Brain Imaging Data Structure, a Format for Organizing and Describing Outputs of Neuroimaging Experiments." *Scientific Data* 3 (1): 160044. https://doi.org/10.1038/sdata.2016.44.

Gousias, Ioannis S., Daniel Rueckert, Rolf a. Heckemann, Leigh E. Dyet, James P. Boardman, a. David Edwards, and Alexander Hammers. 2008. "Automatic Segmentation of Brain MRIs of 2-Year-Olds into 83 Regions of Interest." *NeuroImage* 40 (2): 672–84. https://doi.org/10.1016/j.neuroimage.2007.11.034.

Hajnal, Joseph V., Alan G. Collins, Susan J. White, Jacqueline M. Pennock, Angela Oatridge, Christine J. Baudouin, Ian R. Young, and Graeme M. Bydder. 1993. "Imaging of Human Brain Activity at 0.15 T Using Fluid Attenuated Inversion Recovery (FLAIR) Pulse Sequences." *Magnetic Resonance in Medicine* 30 (5): 650–53. https://doi.org/10.1002/mrm.1910300520.

Hammers, Alexander, Richard Allom, Matthias J. Koepp, Samantha L. Free, Ralph Myers, Louis Lemieux, Tejal N. Mitchell, David J. Brooks, and John S. Duncan. 2003. "Three-Dimensional Maximum Probability Atlas of the Human Brain, with Particular Reference to the Temporal Lobe." *Human Brain Mapping* 19 (4): 224–47. https://doi.org/10.1002/hbm.10123.

Hammers, Alexander, Rolf A. Heckemann, Matthias J. Koepp, John S. Duncan, Jo V. Hajnal, Daniel Rueckert, and Paul Aljabar. 2007. "Automatic Detection and Quantification of Hippocampal Atrophy on MRI in Temporal Lobe Epilepsy: A Proof-of-Principle Study." *NeuroImage* 36 (1): 38–47. https://doi.org/10.1016/j.neuroimage.2007.02.031.

Heckemann, Rolf A., Shiva Keihaninejad, Paul Aljabar, R Gray, Casper Nielsen, Daniel Rueckert, and Joseph V Hajnal. 2011. "Automatic Morphometry in Alzheimer ' s Disease and." *Brain* 56 (4): 1–34.

Huppertz, Hans-Jürgen, Christina Grimm, Susanne Fauser, Jan Kassubek, Irina Mader, Albrecht Hochmuth, Joachim Spreer, and Andreas Schulze-Bonhage. 2005. "Enhanced Visualization of Blurred Gray–White Matter Junctions in Focal Cortical Dysplasia by Voxel-Based 3D MRI Analysis." *Epilepsy Research* 67 (1): 35–50. https://doi.org/https://doi.org/10.1016/j.eplepsyres.2005.07.009.

Huppertz, Hans-Jürgen, Jan Wagner, Bernd Weber, Patrick House, and Horst Urbach. 2011.

"Automated Quantitative FLAIR Analysis in Hippocampal Sclerosis." *Epilepsy Research* 97 (1): 146–56. https://doi.org/https://doi.org/10.1016/j.eplepsyres.2011.08.001.

Iwatsubo, Takeshi, Atsushi Iwata, Kazushi Suzuki, Ryoko Ihara, Hiroyuki Arai, Kenji Ishii, Michio Senda, et al. 2018. "Japanese and North American Alzheimer's Disease Neuroimaging Initiative Studies: Harmonization for International Trials." *Alzheimer's & Dementia : The Journal of the Alzheimer's Association* 14 (8): 1077–87. https://doi.org/10.1016/j.jalz.2018.03.009.

Klein-Koerkamp, Yanica, Rolf A Heckemann, Kylee T Ramdeen, Olivier Moreaud, Sandrine Keignart, Alexandre Krainik, Alexander Hammers, Monica Baciu, and Pascal Hot. 2014. "Amygdalar Atrophy in Early Alzheimer's Disease." *Current Alzheimer Research* 11 (3): 239–52. https://doi.org/10.2174/1567205011666140131123653.

Knudsen, Gitte M, Peter S Jensen, David Erritzoe, William F C Baaré, Anders Ettrup, Patrick M Fisher, Nic Gillings, et al. 2016. "The Center for Integrated Molecular Brain Imaging (Cimbi) Database." *NeuroImage* 124 (Pt B): 1213–19. https://doi.org/10.1016/j.neuroimage.2015.04.025.

Ladefoged, CN, A Hansen, O Henriksen, F Bruun, L Eikenes, S Øen, A Karlberg, L Højgaard, I Law, and Flemming Littrup Andersen. 2020. "AI-Driven Attenuation Correction for Brain PET/MRI: Clinical Evaluation of a Dementia Cohort and Importance of the Training Group Size." *NeuroImage* 222: 117221. https://doi.org/https://doi.org/10.1016/j.neuroimage.2020.117221.

Ladefoged, CN, I. Law, U. Anazodo, K. St. Lawrence, D. Izquierdo-Garcia, C. Catana, N. Burgos, et al. 2017. "A Multi-Centre Evaluation of Eleven Clinically Feasible Brain PET/MRI Attenuation Correction Techniques Using a Large Cohort of Patients." *NeuroImage* 147. https://doi.org/10.1016/j.neuroimage.2016.12.010.

Ladefoged, CN, Lisbeth Marner, Amalie Hindsholm, Ian Law, Liselotte Højgaard, and Flemming Littrup Andersen. 2019. "Deep Learning Based Attenuation Correction of PET/MRI in Pediatric Brain Tumor Patients: Evaluation in a Clinical Setting." *Frontiers in Neuroscience* 13 (JAN): 1–9. https://doi.org/10.3389/fnins.2018.01005.

Merida, Ines, Nicolas Costes, Rolf A. Heckemann, and Alexander Hammers. 2015. "Pseudo-CT Generation in Brain MR-PET Attenuation Correction: Comparison of Several Multi-Atlas Methods." In *EJNMMI Physics*. Vol. 2. https://doi.org/10.1109/ISBI.2015.7164145.

Merida, Ines, Anthonin Reilhac, Jérôme Redouté, Rolf A. Heckemann, Nicolas Costes, and Alexander Hammers. 2017. "Multi-Atlas Attenuation Correction Supports Full Quantification of Static and Dynamic Brain PET Data in PET-MR." *Physics in Medicine and Biology* 62: 2834–2858. https://doi.org/doi.org/10.1088/1361-6560/aa5f6c.

Richardson, M P, K J Friston, S M Sisodiya, M J Koepp, J Ashburner, S L Free, D J Brooks, and J S Duncan. 1997. "Cortical Grey Matter and Benzodiazepine Receptors in Malformations of Cortical Development. A Voxel-Based Comparison of Structural and Functional Imaging Data." *Brain* 120 (11): 1961–73. https://doi.org/10.1093/brain/120.11.1961.

Sapey-Triomphe, Laurie-Anne, Rolf A Heckemann, Nawele Boublay, Jean-Michel Dorey, Marie-Anne Hénaff, Isabelle Rouch, Catherine Padovan, Alexander Hammers, and Pierre Krolak-Salmon. 2015. "Neuroanatomical Correlates of Recognizing Face Expressions in Mild Stages of Alzheimer's Disease." *PloS One* 10 (12): e0143586. https://doi.org/10.1371/journal.pone.0143586.

Sousa, Joao M, Lieuwe Appel, Inés Merida, Rolf A. Heckemann, Nicolas Costes, Mathias Engström, Stergios Papadimitriou, et al. 2020. "Accuracy and Precision of Zero-Echo-Time , Single- and Multi-Atlas Attenuation Correction for Dynamic [11C]PE2I PET-MR Brain Imaging." *Research Square (Preprint)*. https://doi.org/https://doi.org/10.21203/rs.3.rs-42833/v1.

Wei, Longxiao, Kun Guo, Yunbo Li, Zhirui Guo, Chengcheng Gao, Menghui Yuan, and Ming Zhang. 2018. "Construction of a Novel Chinese Normal Brain Database Using 18 F-FDG PET Images and MIMneuro Software, the Initial Application in Epilepsy." *International Journal of Neuroscience* 129 (5): 417–22. https://doi.org/10.1080/00207454.2018.1538138.

Yaakub, SN, Rolf A Heckemann, Simon S Keller, Colm J McGinnity, Bernd Weber, and Alexander Hammers. 2020. "On Brain Atlas Choice and Automatic Segmentation Methods: A Comparison

of MAPER & FreeSurfer Using Three Atlas Databases." *Scientific Reports* 10 (1): 2837. https://doi.org/10.1038/s41598-020-57951-6.

Yaakub, SN, CJ McGinnity, K Beck, I Merida, E Dunston, M Muffoletto, A Qureshi, S Bhattacharya, J MacKewn, and A Hammers. 2019. "Brain PET-MR Attenuation Correction with Deep Learning." In *Journal of Cerebral Blood Flow and Metabolism*, 600–601.

Yaakub, SN, CJ McGinnity, JR Clough, E Kerfoot, N Girard, E Guedj, and A Hammers. 2019. "Pseudo-Normal PET Synthesis with Generative Adversarial Networks for Localising Hypometabolism in Epilepsies BT - Simulation and Synthesis in Medical Imaging." In , edited by Ninon Burgos, Ali Gooya, and David Svoboda, 42–51. Cham: Springer International Publishing.

Yakushev, Igor, Alexander Hammers, Andreas Fellgiebel, Irene Schmidtmann, Armin Scheurich, Hans-Georg Buchholz, Jürgen Peters, Peter Bartenstein, Klaus Lieb, and Mathias Schreckenberger. 2009. "SPM-Based Count Normalization Provides Excellent Discrimination of Mild Alzheimer's Disease and Amnestic Mild Cognitive Impairment from Healthy Aging." *NeuroImage* 44 (1): 43–50. https://doi.org/https://doi.org/10.1016/j.neuroimage.2008.07.015.

Yakushev, Igor, Christian Landvogt, Hans-Georg Buchholz, Andreas Fellgiebel, Alexander Hammers, Armin Scheurich, Irene Schmidtmann, Alexander Gerhard, Mathias Schreckenberger, and Peter Bartenstein. 2008. "Choice of Reference Area in Studies of Alzheimer's Disease Using Positron Emission Tomography with Fluorodeoxyglucose-F18." *Psychiatry Research: Neuroimaging* 164 (2): 143–53. https://doi.org/https://doi.org/10.1016/j.pscychresns.2007.11.004.

Appendix

*Table A1: Individual thresholded T-maps (p < 0.05 FWE) for participants showing significant **increases** in [^{18}F]FDG uptake (hypermetabolism) relative to the other 36 participants (false positives). The analysis consisted in a leave-one-out ANCOVA performed on SPM12 (see Methods for details). For each case, we provide an anatomical or artefactual explanation.*
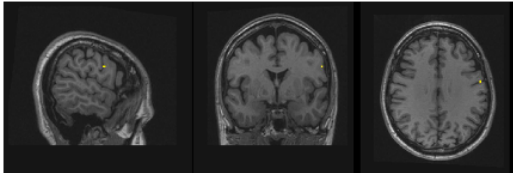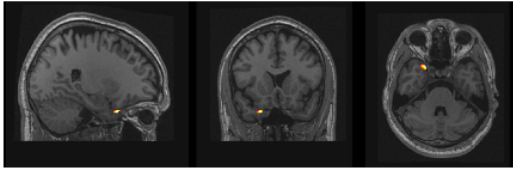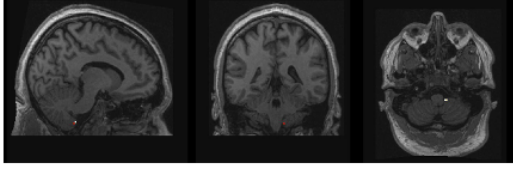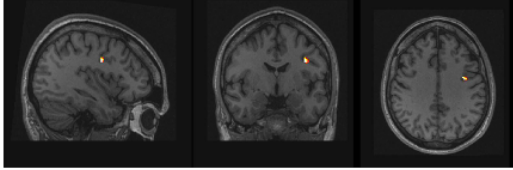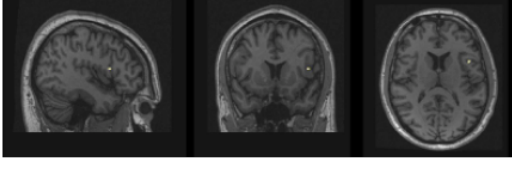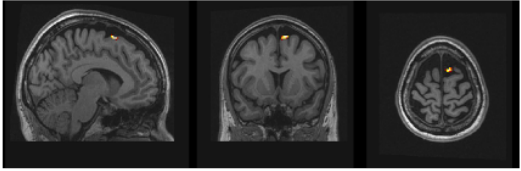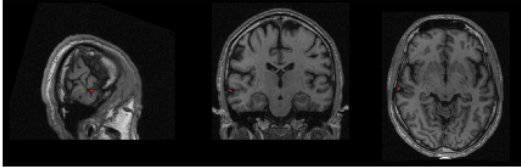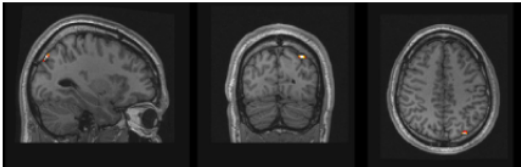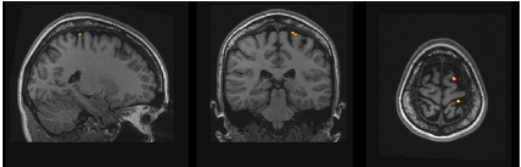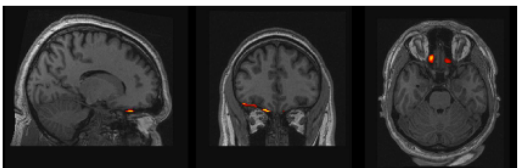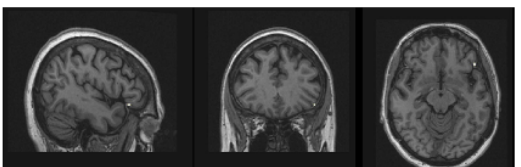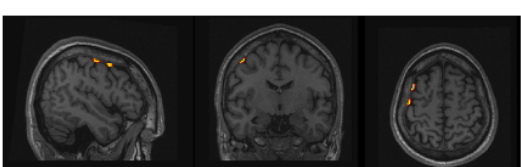
Participant ID	Comment	Illustration
sub-0002	Normalisation artifact (linear artefact seen when lowering threshold)	
sub-0003	Edge of brain	
sub-0010	Extracerebral cluster	
sub-0020	Hypermetabolism due to particular anatomy (grey matter / deep sulcus in this participant, white matter in others)	
sub-0024	Hypermetabolism due to particular anatomy (grey matter / deep sulcus in this participant, white matter in others)	

*Table A2: Individual thresholded T-maps (p < 0.05 FWE) for participants showing significant **decreases** in [^{18}F]FDG uptake (hypometabolism) relative to the other 36 participants (false positives). The analysis consisted in a leave-one-out ANCOVA performed on SPM12 (see Methods for details). For each case, we provide an anatomical or artefactual explanation.*

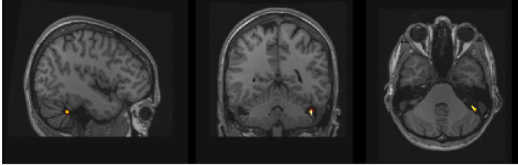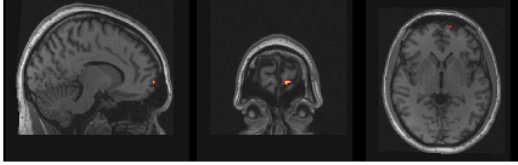| Participant ID	Comment	Illustration
sub-0002	Apparent hypometabolism in deep / wide sulcus in this participant	
sub-0004	Apparent hypometabolism in deep / wide sulcus in this participant	
sub-0005	Apparent hypometabolism in deep / wide sulcus in this participant / linear normalisation artefact	
sub-0007	Apparent hypometabolism in deep / wide sulcus in this participant	
sub-0010	Extracerebral cluster	
sub-0016	Edge of brain	
sub-0017	Apparent hypometabolism in deep / wide sulcus in this participant: Typical artifact in wide Sylvian fissure	
sub-0020	Linear normalisation artefact at edge of brain	
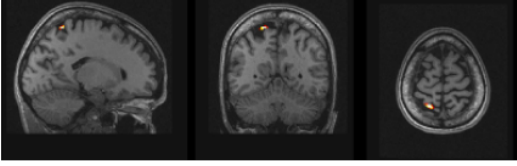
Participant ID	Comment	Illustration
sub-0023	Apparent hypometabolism in unusually wide cerebellar fissure in this participant	
sub-0024	Border effect, possibly linked to imperfect spatial normalisation due to prominent frontal sinuses	
sub-0035	Apparent hypometabolism in deep / wide sulcus in this participant	

Table A3: Abbreviation list of the 83 regions used in the ROI evaluation based on the Hammers_mith atlases (www.brain-development.org / Hammers et al. 2003, Gousias et al. 2008)

Abbreviation	Complete name
Hippocampus_r	Hippocampus (right)
Hippocampus_l	Hippocampus (left)
Amygdala_r	Amygdala (right)
Amygdala_l	Amygdala (left)
Ant_TL_med_r	Anterior temporal lobe, medial part (right)
Ant_TL_med_l	Anterior temporal lobe, medial part (left)
Ant_TL_inf_lat_r	Anterior temporal lobe, lateral part excluding superior temporal gyrus (right)
Ant_TL_inf_lat_l	Anterior temporal lobe, lateral part excluding superior temporal gyrus (left)
G_paraH_amb_r	Parahippocampal and ambient gyri (right)
G_paraH_amb_l	Parahippocampal and ambient gyri (left)
G_s_t_cent_r	Superior temporal gyrus, central part (right)
G_s_t_cent_l	Superior temporal gyrus, central part (left)
G_tem_midin_r	Middle and inferior temporal gyrus (right)
G_tem_midin_l	Middle and inferior temporal gyrus (left)
G_occtem_la_r	Fusiform (lateral occipitotemporal) gyrus (right)
G_occtem_la_l	Fusiform (lateral occipitotemporal) gyrus (left)
Cerebellum_r	Cerebellum (right)
Cerebellum_l	Cerebellum (left)
Brainstem	Brainstem
Insula_l	Insula (left)
Insula_r	Insula (right)
OL_rest_lat_l	Lateral remainder of occipital lobe (left)
OL_rest_lat_r	Lateral remainder of occipital lobe (right)
G_cing_a_s_l	Cingulate gyrus, anterior part (left)
G_cing_a_s_r	Cingulate gyrus, anterior part (right)
G_cing_p_l	Gyrus cinguli, posterior part (left)
G_cing_p_r	Gyrus cinguli, posterior part (right)
FL_mid_fr_G_l	Middlle frontal gyrus (left)
FL_mid_fr_G_r	Middlle frontal gyrus (right)
PosteriorTL_l	Posterior temporal lobe (left)
PosteriorTL_r	Posterior temporal lobe (right)
PL_rest_l	Inferiolateral remainder of parietal lobe (left)
PL_rest_r	Inferiolateral remainder of parietal lobe (right)
CaudateNucl_l	Caudate nucleus (left)
CaudateNucl_r	Caudate nucleus (right)
NuclAccumb_l	Nucleus accumbens (left)
NuclAccumb_r	Nucleus accumbens (right)
Putamen_l	Putamen (left)
Putamen_r	Putamen (right)
Thalamus_l	Thalamus (left)
Thalamus_r	Thalamus (right)
Pallidum_l	Pallidum (left)
Pallidum_r	Pallidum (right)
Corp_Callosum	Corpus callosum
LatVent_excl_TH_r	Lateral ventricle (excluding temporal horn) (right)
LatVent_excl_TH_l	Lateral ventricle (excluding temporal horn) (left)
BodyVentricle_r	Lateral ventricle, body of right ventricle
BodyVentricle_l	Lateral ventricle, body of left ventricle
ThirdVentricl	Third ventricle

FL_precen_G_l	Precentral gyrus (left)
FL_precen_G_r	Precentral gyrus (right)
FL_strai_G_l	Straight gyrus (left)
FL_strai_G_r	Straight gyrus (right)
FL_OFC_AOG_l	Anterior orbital gyrus (left)
FL_OFC_AOG_r	Anterior orbital gyrus (right)
FL_i_fr_G_l	Inferior frontal gyrus (left)
FL_i_fr_G_r	Inferior frontal gyrus (right)
FL_s_fr_G_l	Superior frontal gyrus (left)
FL_s_fr_G_r	Superior frontal gyrus (right)
PL_postce_G_l	Postcentral gyrus (left)
PL_postce_G_r	Postcentral gyrus (right)
PL_s_pa_G_l	Superior parietal gyrus (left)
PL_s_pa_G_r	Superior parietal gyrus (right)
OL_ling_G_l	Lingual gyrus (left)
OL_ling_G_r	Lingual gyrus (right)
OL_cuneus_l	Cuneus (left)
OL_cuneus_r	Cuneus (right)
FL_OFC_MOG_l	Medial orbital gyrus (left)
FL_OFC_MOG_r	Medial orbital gyrus (right)
FL_OFC_LOG_l	Lateral orbital gyrus (left)
FL_OFC_LOG_r	Lateral orbital gyrus (right)
FL_OFC_POG_l	Posterior orbital gyrus (left)
FL_OFC_POG_r	Posterior orbital gyrus (right)
S_nigra_l	Substantia nigra (left)
S_nigra_r	Substantia nigra (right)
Subgen_antCing_l	Subgenual frontal cortex (left)
Subgen_antCing_r	Subgenual frontal cortex (right)
Subcall_area_l	Subcallosal area (left)
Subcall_area_r	Subcallosal area (right)
Presubgen_antCing_l	Pre-subgenual frontal cortex (left)
Presubgen_antCing_r	Pre-subgenual frontal cortex (right)